

## Spectral Analysis of the Flare of 1998 November 11 based on the Multi-cloud Model

Xiao-Ma Gu<sup>1,3</sup> \* and Ming-De Ding<sup>2</sup>

<sup>1</sup> Yunnan Observatory, National Astronomical Observatories, CAS, Kunming 650011

<sup>2</sup> Department of Astronomy, Nanjing University, Nanjing 210093

<sup>3</sup> United Laboratory of Optical Astronomy, Chinese Academy of Sciences

Received 2001 July 14; accepted 2001 December 18

**Abstract** We have obtained 2D spectra of H $\alpha$  and CaII  $\lambda$  8542Å for the flare of 1998 November 11, and derived its 2D velocity field and integrated intensity field. The velocity distribution shows that the red-shift and blue-shift velocities lie respectively in the northern and southern parts of the flare and that the maximum velocity seems to be located in two footpoints of the flare loop system. The integrated intensity distribution shows that the CaII  $\lambda$  8542Å line is formed at a lower height than the H $\alpha$  line. we used ‘multi-cloud model’ (MCM) to obtain four parameters for the two lines (Doppler width,  $\Delta\lambda_D$ , Doppler shift,  $\Delta\lambda_0$ , line source function,  $S$ , and optical depth at the line center,  $\tau_0$ ). We also estimated the column number densities of hydrogen at the second level,  $N_2$ , and of the ionized calcium at the third level,  $N_3$ , as well as the kinetic temperature,  $T_c$ . The wide H $\alpha$  profile at the loop top may be explained by an overlapping of two or more elementary profiles. It is shown that the uncertainty in calibration does not affect the derived Doppler shift and line broadening, only the source function and optical depth.

**Key words:** Sun: activity — Sun: flares — methods: data analysis

### 1 INTRODUCTION

Although coronal mass ejection (CME) as a representation of solar eruptive events has become a most popular subject in solar physics since the rapid development of space observations, the study of solar flares remains attractive. Modern space and ground-based observations show that solar flares are loop phenomena; in general, they are composed of several loops forming a loop system. There are two kinds of loops: X-ray loops and post-flare loops; the former are hot loops observed with X-ray telescopes on board spacecraft, while the latter are cool loops observed in H $\alpha$  line.

To reveal the mechanism of solar flares as well as their dynamic characteristics, cool and hot flare loops and other eruptive events associated with flares have been extensively studied by many authors (e.g., Gu et al. 1992, 1997; Ding et al. 1995, 1999; Chen et al. 1999; Švestka et al. 1987; Fang et al. 1995, 1998; Schmieder et al. 1995a, 1995b, 1996; Li et al.

---

\* E-mail: ssg@public.km.yn.cn

1993, 1995; Lin et al. 1995; Heinzel et al. 1992; van Driel-Gesztelyi et al. 1996; Wiik et al. 1996; Zhong et al. 1991, 1995). Spectral analysis is an important means of studying solar flare loops. Some basic parameters, such as Doppler shift and Doppler width of the line under consideration, optical depth, and the line source function etc. in flare loops may be obtained from the spectral analysis. Especially, the two-dimensional spectra are quite suitable for the study of global properties of flares; one can obtain not only the two-dimensional distributions of physical parameters but also their dynamical evolution process.

However, the method of spectral analysis itself is another key issue yet to be investigated. Traditional method is based on symmetric profile, but a number of observations show that the profiles of solar flares are usually asymmetric. This makes the traditional method inappropriate for analyzing the flare profiles. The method of ‘cloud model’ (Beckers 1964) and that of ‘differential cloud models’ (DCM1, DCM2), which were proposed by Mein and Mein (1988), are again only suitable for symmetric profiles. The basic scenario of chromospheric condensation has successfully explained the asymmetric profiles in disk flares (e.g., Gan et al. 1993; Ding & Fang 1997), but it is unsuitable for limb flares. To resolve this problem, a method of ‘multi-cloud model’ (MCM) was proposed by Gu et al. (1992, 1995, 1996) on the basis of the ‘cloud model’ and the DCM1 and DCM2. The MCM method has been applied to many asymmetric profiles of flares, prominences, and surges etc. (Gu et al. 1994, 1997; Li et al. 1993, 1998; Dun et al. 1998, 2000).

On 1998 November 11, a limb flare was observed by the solar tower of Nanjing University with an imaging spectrograph in the  $H\alpha$  and  $\text{CaII } \lambda 8542\text{\AA}$  lines. Ding et al. (1999) analyzed preliminarily the 2D flare spectra obtained. Fang et al. (2000) proposed a new broadening mechanism of line profiles so as to explain the very broad  $H\alpha$  profile at the loop top. In this paper, we study the velocity fields, intensity fields and other physical quantities of the limb flare using the MCM method. We also estimate the effects of calibration error and discuss another possible way of broadening line profiles.

## 2 OBSERVATIONS AND DATA REDUCTION

The flare occurred at the solar northwest limb ( $N25^\circ$ ,  $W86^\circ$ ) on 1998 November 11. According to the *Solar Geophysical Data*, the flare began at 02:10 UT, reached its maximum at 02:15 UT and ended at 02:18 UT. The  $H\alpha$ /soft X-ray importance is SF/C3.2. The corresponding active region is NOAA/USAF 8375. The event was characterized by the formation of flaring loops above the solar limb. It was observed with the solar imaging spectrograph installed on the solar tower of Nanjing University. The flare was analyzed preliminarily by Ding et al. (1999, hereafter “Paper I”), the details of the observation and the instrument were given by Ding et al. in Paper I and Huang et al. (1995), Ding et al. (1995). Figure 1 shows the monochromatic image of the flare in  $H\alpha$ , reconstructed from the 3D data array. Figure 1 also marks out 36 small squares which cover nearly the whole flare; for each square, the  $H\alpha$  and  $\text{CaII } \lambda 8542\text{\AA}$  line profiles are given in Figure 3 in relative units.

The flare was also recorded by the soft X-ray telescope (SXT) aboard the *Yohkoh* satellite, and its soft X-ray image is given in Figure 2. The soft X-ray image is quite different from the  $H\alpha$  image: there are two bright cores near the solar limb without evident loop-like shape; there is asymmetry between the two cores: the major core lies in the northern part of the active region, probably with S magnetic polarity, while the minor one lies in the southern part, corresponding to N polarity.

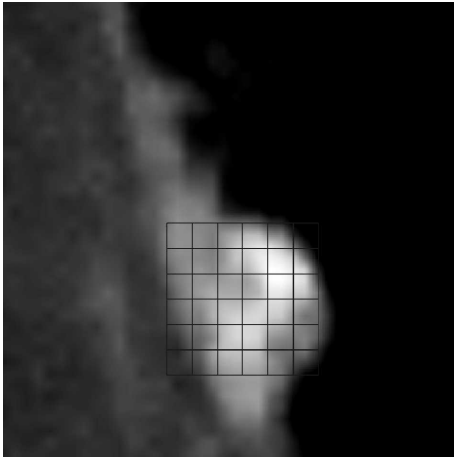


Fig. 1 Monochromatic image of  $H\alpha$  reproduced from the 2D spectra at 02:14:38 UT. The field of view is  $60'' \times 60''$ . North is up, west is to the right.

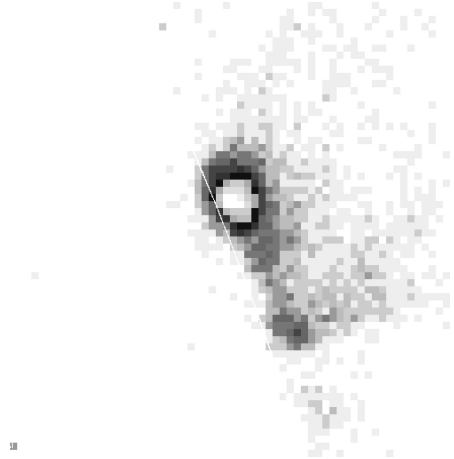


Fig. 2 Soft X-ray image of the limb flare loop of November 11, 1998, observed by *Yohkoh* at 02:11 UT. The white line denotes the solar limb. North is up, west is to the right.

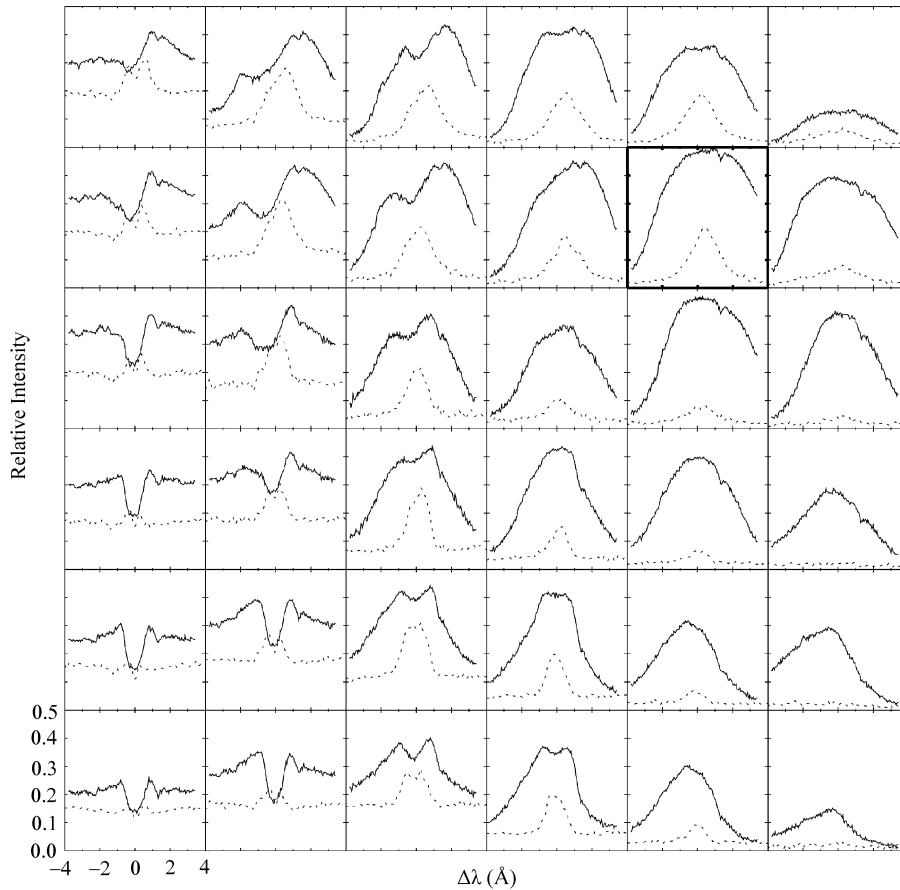


Fig. 3 Line profiles of  $H\alpha$  (solid lines) and  $\text{CaII } \lambda$  8542Å (dashed lines) at 02:14:38 UT. The units of the intensities are arbitrary. Each box has a one-to-one correspondence to each small square in Fig. 1.

To fit the line profiles, we need first to make a calibration for absolute line intensities. Unfortunately, we missed making spectral observations at the disk center, therefore, the calibration was based on spectra close to the limb ( $\mu \approx 0.1$ ), corrected for limb darkening. This procedure unavoidably decreased the accuracy of the calibration. The uncertainty of the absolute intensity is estimated to be  $\pm 20\%$ . However, it is expected that the uncertainty does not affect the Doppler shift or the line broadening. In this paper, the profiles given in Fig. 3 are further calibrated to absolute units ( $\text{erg cm}^{-2} \text{s}^{-1} \text{\AA}^{-1}$ ).

Our aim in this paper is to analyze the spectra within the flare loop system shown in Fig. 3 to obtain the kinetic features and physical properties of the flare as well as to explain the line broadening in a different manner. The effect of calibration error on the physical parameters is being taken into account.

### 3 METHOD OF DATA ANALYSIS

#### 3.1 Method of Profile Weight Center

To determine the average line-of-sight velocity, a method of profile weight center is considered here. The area enclosed by the profile and the wavelength axis is divided into four equal parts by three wavelength points:  $\lambda_1, \lambda_2$  and  $\lambda_3$  (see Fig. 4);  $\lambda_2$  obviously marks the position of the weight center of the profile. We may take the difference between  $\lambda_2$  and the theoretical line center as the Doppler shift,  $\Delta\lambda$ , of the loop system:  $\Delta\lambda = \lambda_2 - \lambda_0$ ; hence an average Doppler velocity  $V_{\parallel} = c\Delta\lambda/\lambda_0$ , where  $c$  is the light velocity and  $\lambda_0$  is the theoretical wavelength of the line center. The integrated intensity,  $E$ , is

$$E = \int_0^{\infty} I_{\lambda} d\lambda. \quad (1)$$

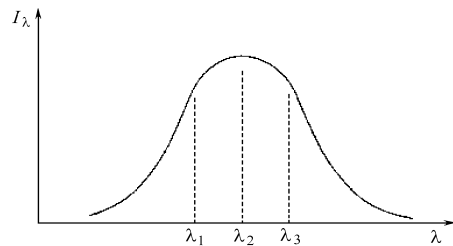


Fig. 4 Schematic diagram showing the method of weight center.  $\lambda_1, \lambda_2$  and  $\lambda_3$  are three wavelength points which divide the area enclosed by the profile and the wavelength axis into four equivalent parts.

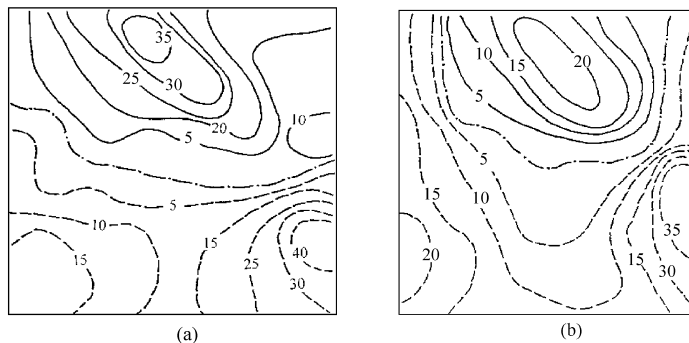


Fig. 5 Velocity contours of the flare loop system for (a)  $\text{H}\alpha$  line; (b)  $\text{CaII } \lambda 8542\text{\AA}$  line. Solid and dashed lines refer to red-shift and blue-shift velocities, respectively; dot-dashed lines are zero velocity lines. The units of velocity is  $\text{km s}^{-1}$ .

V and E were computed for the H $\alpha$  and CaII  $\lambda$  8542Å lines and 2D distributions of the two parameters are shown in Figs. 5 and 6, respectively.

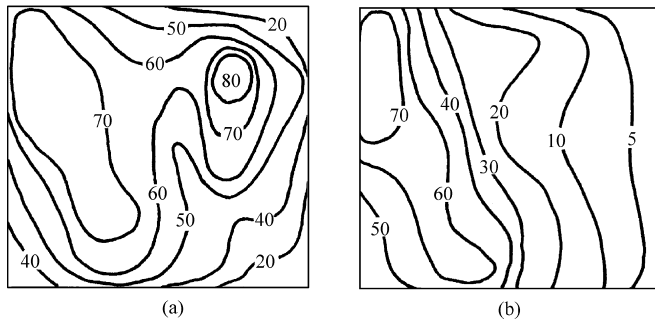


Fig. 6 Contours of integrated intensity for (a) H $\alpha$  line and (b) CaII  $\lambda$  8542Å line, in units of  $10^5 \text{ erg cm}^{-2} \text{ sr}^{-1} \text{ s}^{-1}$ .

### 3.2 ‘Multi-cloud model’ Method

Figure 3 shows that most of the H $\alpha$  and CaII  $\lambda$  8542Å profiles are asymmetric. The traditional methods of the ‘cloud model’ (Beckers 1964) and DCMs (Mein and Mein 1988) are invalid for an asymmetric profile in a limb flare. So we propose a method of ‘multi-cloud model’ (MCM) (Gu et al. 1992, 1995, 1996). We consider an asymmetric (non-Gaussian) profile to be a result of overlapping of several symmetric (Gaussian) profiles (i.e. elementary profiles) along the line of sight. These elementary profiles are assumed to be formed in some small radiative elements (the so-called ‘clouds’) which have different or identical physical properties; and, in these ‘clouds’, the source function and mass motion velocity are assumed to be independent of depth. Some researches have shown that a main way of producing an asymmetric profile is that the source function and the velocity field within the plasma both vary non-linearly with depth (Ye et al. 1985; Chen et al. 1987). Our method is based on a simplification of this scenario. The asymmetry of the profile is from the relative Doppler shifts of different clouds. The profile is simulated as follows:

$$I_\lambda = \sum_{j=1}^m S_j (1 - e^{-\tau_j}) \exp\left(-\sum_{i=0}^{j-1} \tau_i\right), \quad (2)$$

where we let  $\tau_0 = 0$ , while the optical depth of the  $j^{\text{th}}$  radiative element is

$$\tau_j = \tau_{0,j} \exp\left[-\left(\frac{\Delta\lambda - \Delta\lambda_j}{\Delta\lambda_{D,j}}\right)^2\right], \quad (3)$$

where  $m$  is the number of elementary profiles,  $S_j$ ,  $\tau_{0,j}$ ,  $\Delta\lambda_j = \lambda V_j/c$  and  $\Delta\lambda_{D,j}$  are the source function, optical depth at the line center, Doppler shift and Doppler width of the  $j^{\text{th}}$  radiative element, respectively. Using the method and some mathematical manipulations (Li et al. 1992, 1993, 1994), we can derive  $S$ ,  $\tau_0$ ,  $\Delta\lambda_D$  and  $\Delta\lambda_0$  for the two lines by fitting the observed profiles by Eq.(2). Figure 7 gives the results of profile fitting for the H $\alpha$  and CaII  $\lambda$  8542Å lines at two spatial sites: (1, 3) and (2, 5) (see Figs. 1 and 3). Position (1, 3) is at the north foot point and (2, 5) at the top of the flare loop (for the H $\alpha$  image). The derived parameters and their rms errors are given in Table 1 for four sites: (2, 5), (1, 3), (5, 4) and (6, 4). Here,  $S_1$  and  $S_2$  are given in absolute units.

**Table 1** Physical Parameters Derived from the MCM Method

Sites	(2, 5)	(1, 3)	(5, 4)	(6, 4)
Parameters				
$S_1^{\text{H}\alpha}$ ( $10^6$ )	$1.372 \pm 0.206$	$1.475 \pm 0.221$	$1.153 \pm 0.173$	$0.997 \pm 0.150$
$S_2^{\text{H}\alpha}$ ( $10^6$ )	$0.846 \pm 0.127$	$1.200 \pm 0.180$	$1.021 \pm 0.153$	$1.310 \pm 0.197$
$S_1^{\text{Ca}}$ ( $10^6$ )	$7.452 \pm 1.118$	$7.641 \pm 1.146$	$5.166 \pm 0.775$	$4.705 \pm 0.706$
$\tau_{0,1}^{\text{H}\alpha}$	$3.736 \pm 0.486$	$1.552 \pm 0.202$	$7.294 \pm 0.948$	$23.891 \pm 3.106$
$\tau_{0,2}^{\text{H}\alpha}$	$2.048 \pm 0.266$	$1.300 \pm 0.169$	$1.450 \pm 0.188$	$0.912 \pm 0.119$
$\tau_0^{\text{Ca}}$	$0.211 \pm 0.027$	$0.212 \pm 0.028$	$0.221 \pm 0.029$	$0.238 \pm 0.031$
$\Delta\lambda_{\text{D},1}^{\text{H}\alpha}$ ( $\text{\AA}$ )	$2.392 \pm 0.012$	$1.266 \pm 0.006$	$0.728 \pm 0.004$	$0.636 \pm 0.003$
$\Delta\lambda_{\text{D},2}^{\text{H}\alpha}$ ( $\text{\AA}$ )	$0.944 \pm 0.005$	$1.591 \pm 0.008$	$2.480 \pm 0.012$	$2.599 \pm 0.013$
$\Delta\lambda_{\text{D}}^{\text{Ca}}$ ( $\text{\AA}$ )	$1.315 \pm 0.007$	$1.345 \pm 0.007$	$0.887 \pm 0.004$	$0.920 \pm 0.005$
$\Delta\lambda_{0,1}^{\text{H}\alpha}$ ( $\text{\AA}$ )	$0.605 \pm 0.009$	$1.796 \pm 0.027$	$-0.079 \pm 0.001$	$-0.165 \pm 0.002$
$\Delta\lambda_{0,2}^{\text{H}\alpha}$ ( $\text{\AA}$ )	$0.735 \pm 0.011$	$-0.731 \pm 0.011$	$-0.553 \pm 0.008$	$-0.678 \pm 0.010$
$\Delta\lambda_0^{\text{Ca}}$ ( $\text{\AA}$ )	$0.431 \pm 0.006$	$0.552 \pm 0.008$	$-0.093 \pm 0.001$	$-0.098 \pm 0.001$
rms	0.149 ( $\text{H}\alpha$ )	0.303 ( $\text{H}\alpha$ )	0.163 ( $\text{H}\alpha$ )	0.204 ( $\text{H}\alpha$ )
( $\leq 10^{-2}$ )	0.726 ( $\text{CaII}$ )	0.351 ( $\text{CaII}$ )	0.352 ( $\text{CaII}$ )	0.272 ( $\text{CaII}$ )

Note: The unite of  $S$  is  $\text{erg cm}^{-2} \text{s}^{-1} \text{sr}^{-1} \text{\AA}^{-1}$ .

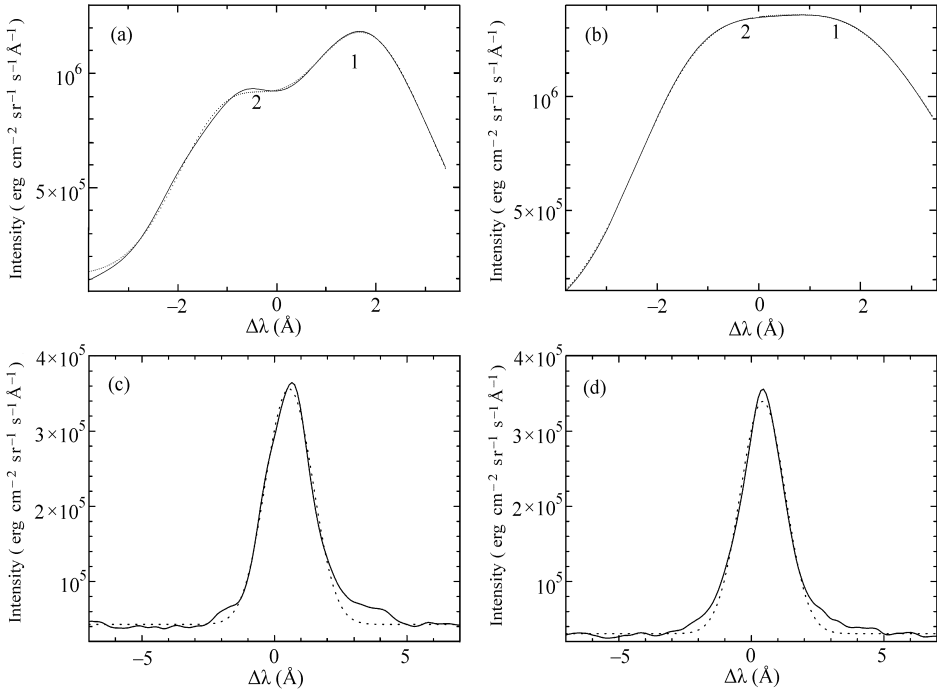


Fig. 7 Spectral profiles of the flare loop system. Solid lines represent observed profiles and dashed lines computed ones with the MCM method. (a) and (b) are for  $\text{H}\alpha$  profiles at the footpoint (1, 3) and at the top (2, 5) sites, respectively; (c) and (d) are for  $\text{CaII } \lambda 8542 \text{\AA}$  profiles at the footpoint (1, 3) and at the top (2, 5) sites, respectively.

#### 4 VELOCITY AND INTENSITY FIELDS

Figures 5 and 6 are 2D contours of velocity and intensity in the 36 squares of Fig. 1. In Figs. 5 and 6, panel (a) is for the H $\alpha$  line and (b) for the CaII  $\lambda$  8542Å line. One may find from Fig. 5a that there is a red-shift region in the northern part and a blue-shift region in the southern part, between which a zero velocity line runs across from east to west; the biggest red-shift velocity is 35 km s<sup>-1</sup> and the biggest blue-shift velocity is 40 km s<sup>-1</sup> for H $\alpha$ , located respectively at (1, 3) and (5, 6). For the CaII  $\lambda$  8542Å line, the values are 20 km s<sup>-1</sup> and 35 km s<sup>-1</sup> (Fig. 5b) occurring in (1, 3), (2, 4) and (4, 6), (5, 6), respectively. From the monochromatic images (Fig. 1), we may infer that the southern leg of the loops is toward, and the northern one away from the observer. It probably indicates that matter in the loops falls down from the loop top along its legs to the footpoints where the velocity reaches a maximum. Fig. 5b gives also a similar configuration of material motion; the distance between the two footpoints of the CaII  $\lambda$  8542Å loops seems shorter than that of the H $\alpha$  loops, which means that the CaII  $\lambda$  8542(Å) loops are lower than the H $\alpha$  loops. This is also confirmed by Figs. 6a and 6b, which show that the CaII  $\lambda$  8542Å line is formed at a much lower level than the H $\alpha$  line. The maximum value of  $E$ , 80 ( $\times 10^5$  erg cm<sup>-2</sup> sr<sup>-1</sup> s<sup>-1</sup>), in Fig. 6a is at the loop top, site (2, 5), for the H $\alpha$  loop system. It is interesting that the position of maximum profile asymmetry and that of maximum intensity do not coincide. This is always the case for both the H $\alpha$  and CaII  $\lambda$  8542Å lines. This result is consistent with that obtained by Mein et al. (1997) who analyzed the same lines.

#### 5 COMPUTATION OF PHYSICAL PARAMETERS

We have obtained the values of  $S$ ,  $\Delta\lambda_D$ ,  $\tau_0$ , and  $\Delta\lambda_0$  by fitting the observed profiles using the MCM method. It is found from Fig. 7 that the theoretical profiles are all in good agreement with observed ones except for the line wings. This implies that the method itself is valid and the parameters derived with this method are meaningful. Therefore, allowing for departure from LTE while neglecting stimulated emission, we can estimate the column number density of the hydrogen/calcium atom at the second/third level along the line of sight, the kinetic temperature (in fact, the brightness temperature) and the micro-turbulence velocity using the following relations:

$$N_i = \frac{m_e c^2}{\sqrt{\pi} e^2 \lambda_0^2 f_{ij}} \tau_0 \Delta\lambda_D, \quad (4)$$

$$T_c = \frac{\frac{hc}{\lambda_0 k}}{\ln\left[\frac{b_j}{b_i} \left(1 + \frac{2hc^2}{\lambda_0^5 S}\right)\right]}, \quad (5)$$

and

$$V_t \approx \sqrt{\frac{\Delta\lambda_D^2 c^2}{\lambda_0^2} - \frac{2kT_c}{m_i}}, \quad (6)$$

where  $m_i$  is the atomic mass; for H $\alpha$ ,  $i = 2$ ,  $j = 3$ ; for CaII  $\lambda$  8542Å,  $i = 3$ ,  $j = 5$ ;  $b_i$  and  $b_j$  are departure coefficients which are related to the temperature and density of the flare loops. When the hydrogen number density is 10<sup>11</sup> cm<sup>-3</sup> and the temperature is 10 000 K, we obtain, using full NLTE computations,  $b_2 = 108$ ,  $b_3 = 7.5$  for H $\alpha$ . The results computed from H $\alpha$  for the four sites are listed in Table 2 (denoted with a superscript ‘H $\alpha$ ’ in the corresponding parameters). For the CaII  $\lambda$  8542Å line, however, owing to its much lower height of formation,

the deviation from LTE should be much less and we still adopt the assumption of LTE here. The results from this line are also listed in Table 2 (superscripted ‘Ca’).

**Table 2** Physical Parameters Computed with Eqs. (4)–(6)

Sites	(2, 5)	(1, 3)	(5, 4)	(6, 4)
Parameters				
$N_2(N_{2,1}^{\text{H}\alpha} + N_{2,2}^{\text{H}\alpha})$	7.935	2.945	6.501	12.822
$N_{2,1}^{\text{H}\alpha} (10^{13} \text{cm}^{-2})$	$6.524 \pm 0.881$	$1.434 \pm 0.194$	$3.876 \pm 0.523$	$11.092 \pm 1.497$
$N_{2,2}^{\text{H}\alpha} (10^{13} \text{cm}^{-2})$	$1.411 \pm 0.190$	$1.510 \pm 0.204$	$2.625 \pm 0.354$	$1.730 \pm 0.233$
$N_3^{\text{Ca}} (10^{13} \text{cm}^{-2})$	$1.440 \pm 0.194$	$1.48 \pm 0.200$	$1.02 \pm 0.138$	$1.14 \pm 0.154$
$V_{\parallel,1}^{\text{H}\alpha} (\text{km s}^{-1})$	$27.225 \pm 0.408$	$77.490 \pm 1.162$	$-3.555 \pm 0.053$	$-7.425 \pm 0.111$
$V_{\parallel,2}^{\text{H}\alpha} (\text{km s}^{-1})$	$33.075 \pm 0.496$	$-22.14 \pm 0.332$	$-24.885 \pm 0.373$	$-30.51 \pm 0.485$
$V_{\parallel}^{\text{Ca}} (\text{km s}^{-1})$	$15.14 \pm 0.227$	$19.39 \pm 0.291$	$-3.27 \pm 0.049$	$-3.44 \pm 0.052$
$T_{c,1}^{\text{H}\alpha} (10^4 \text{K})$	$1.363 \pm 0.125$	$1.475 \pm 0.146$	$1.232 \pm 0.103$	$1.14 \pm 0.088$
$T_{c,2}^{\text{H}\alpha} (10^4 \text{K})$	$1.051 \pm 0.075$	$1.320 \pm 0.118$	$1.154 \pm 0.090$	$1.326 \pm 0.119$
$T_c^{\text{Ca}} (10^4 \text{K})$	$1.117 \pm 0.086$	$1.132 \pm 0.088$	$0.934 \pm 0.065$	$0.895 \pm 0.060$
$V_{t,1}^{\text{H}\alpha} (\text{km s}^{-1})$	$109.309 \pm 0.455$	$41.700 \pm 0.092$	$33.1 \pm 0.072$	$28.8 \pm 0.113$
$V_{t,2}^{\text{H}\alpha} (\text{km s}^{-1})$	$43.00 \pm 0.086$	$90.2 \pm 0.187$	$113.3 \pm 0.483$	$118.7 \pm 0.512$
$V_t^{\text{Ca}} (\text{km s}^{-1})$	$46.12 \pm 0.242$	$47.17 \pm 0.242$	$31.07 \pm 0.136$	$32.24 \pm 0.172$

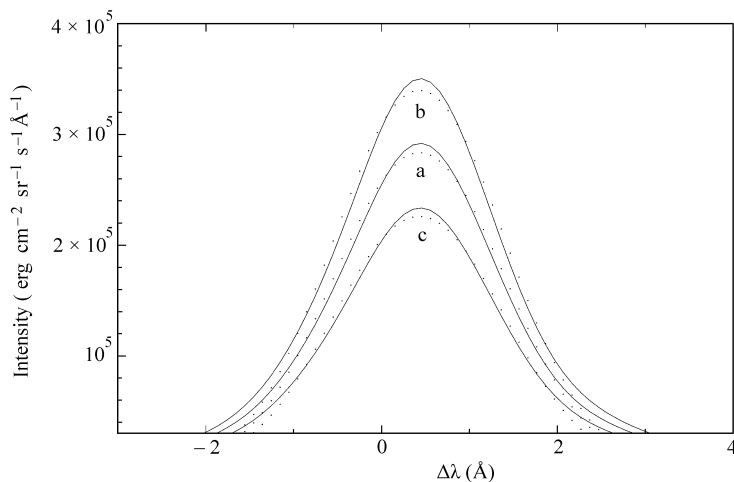


Fig. 8 Profiles of (a)  $I_{\lambda}^{\text{obs}}$ , (b)  $(1 + 20\%)I_{\lambda}^{\text{obs}}$ , and (c)  $(1 - 20\%)I_{\lambda}^{\text{obs}}$ . Solid lines refer to observed profiles, while dashed lines to computed ones.

## 6 ERROR ANALYSIS

Considering that the calibration is not based on the observation at the center of the solar disk, it is likely that there are errors or uncertainties in the calibrated profiles. We assume that

the upper limit of the error in the calibrated intensity is about 20 percent. In order to test the effect of the calibration error on the fitted results, we perform a new fitting for the profiles of  $(1\pm 20\%)I_\lambda^{\text{obs}}$  for the CaII  $\lambda$  8542Å line (Fig. 8). Table 3 shows the results for four sites. One can find that the calibration error affects mainly the source function,  $S$ , and the optical depth at the line center,  $\tau_0$ , while it has less influence on the Doppler shift,  $\Delta\lambda_0$ , and the line width,  $\Delta\lambda_D$ . Denote by  $X_i$  ( $i=1, 2, 3$  and  $4$ ) the four parameters ( $S$ ,  $\tau_0$ ,  $\Delta\lambda_D$  and  $\Delta\lambda_0$ ) and by  $\Delta X_i$  their relative changes ( $\delta S$ ,  $\delta\tau_0$ ,  $\delta\Delta\lambda_D$  and  $\delta\Delta\lambda_0$ ) defined by

$$\Delta X_i = \frac{X'_i - X_i}{X_i}, \quad (7)$$

where  $X'_i$  is the fitted parameter for the profiles of  $(1\pm 20\%)I_\lambda^{\text{obs}}$ . We obtain the relative variations of each parameter (in percent) listed in Table 3. It shows that the relative error of  $S$  may range from 4% to 33%, with an average of 15%; the error of  $\tau_0$  ranges from 4% to 23%, with an average of 13%. These accuracies are comparable to that of photograph calibration. It is found from Table 3 that the relative error of  $S$  from the profile of  $(1+20\%)I_\lambda^{\text{obs}}$  is smaller than that from the profile of  $(1-20\%)I_\lambda^{\text{obs}}$ . However for  $\tau_0$ , the result is the other way round. This is because of the fact that the product of  $S$  and  $\tau_0$  is related to the line intensity for the optically thin case. Based on Eqs.(4), (5) and (6), we derive the relative errors of  $N_i$ ,  $T_c$  and  $V_t$ ,  $\delta N_i$ ,  $\delta T_c$  and  $\delta V_t$ . The relative errors of the parameters are also listed in Table 2.

**Table 3** Effects of Calibration Error on the Derivation of Parameters for CaII  $\lambda$ 8542Å Line

Sites ( $i, j$ )	Intensity $I \pm 20\%$	$S$	$\delta S$ (%)	$\tau_0$	$\delta\tau_0$ (%)	$\Delta\lambda_D$ (Å)	$\delta\Delta\lambda_D$ (%)	$\Delta\lambda_0$ (Å)	$\delta\Delta\lambda_0$ (%)	Error (E-2)
1, 3	I+20	7.952	4.07	0.248	16.98	1.335	0.74	0.554	0.36	0.438
	I	7.641		0.212		1.345		0.552		0.351
	I-20	5.669	25.81	0.230	8.49	1.337	0.59	0.550	0.36	0.286
2, 5	I+20	7.819	4.92	0.245	16.11	1.309	0.46	0.431	0.00	0.876
	I	7.452		0.211		1.315		0.431		0.726
	I-20	4.933	33.80	0.260	23.22	1.298	1.29	0.428	0.70	0.591
5, 4	I+20	5.390	4.34	0.259	17.19	0.887	0.00	-0.089	4.30	0.437
	I	5.166		0.221		0.887		-0.093		0.352
	I-20	4.612	10.72	0.196	11.31	0.890	0.34	-0.091	2.15	0.275
6, 4	I+20	5.234	11.24	0.258	8.40	0.918	0.22	-0.099	1.12	0.33
	I	4.705		0.238		0.920		-0.098		0.272
	I-20	3.605	23.38	0.249	4.62	0.920	0.00	-0.100	2.15	0.221

Note: The unit of  $S$  is:  $10^6 \text{ erg cm}^{-2} \text{ sr}^{-1} \text{ \AA}^{-1} \text{ s}^{-1}$ .

## 7 SUMMARY AND DISCUSSION

We have analyzed the 2D spectra of H $\alpha$  and CaII  $\lambda$  8542Å lines for the flare loop system and obtained the 2D velocity and intensity fields. The velocity distribution shows that matter in the loops falls down from its top towards its feet along the legs. A distribution of integrated intensity shows that the forming height of the CaII  $\lambda$  8542Å line is much lower than that of H $\alpha$  line. We derive four parameters ( $S$ ,  $V$ ,  $\Delta\lambda_D$  and  $\tau_0$ ) with the MCM method for four sites in the flare. The column number density, temperature and turbulent velocity are calculated

and estimated. The results show that  $N_2$ , the population of hydrogen at the second level, is  $(2.9\text{--}12.8) \times 10^{13} \text{ cm}^{-2}$ , it is the sum of the column number densities of two clouds along the line of sight;  $N_3$ , the population of ionized calcium at the third level, is  $(1.0\text{--}1.5) \times 10^{13} \text{ cm}^{-2}$ ; the average values are  $7.6 \times 10^{13}$  and  $1.3 \times 10^{13} \text{ cm}^{-2}$ , respectively. The value of  $T_c$  is  $1.3 \times 10^4 \text{ K}$  for  $\text{H}\alpha$  and  $1.0 \times 10^4 \text{ K}$  for  $\text{CaII } \lambda 8542\text{\AA}$ . A turbulence velocity  $V_t$  of  $47.4 \text{ km s}^{-1}$  is estimated for  $\text{H}\alpha$  and of  $40 \text{ km s}^{-1}$  for  $\text{CaII } \lambda 8542\text{\AA}$ . The uncertainty of calibration of absolute intensity is estimated to be  $\pm 20\%$ ; it affects mainly  $S$  and  $\tau_0$  to an average deviation of 15% and 13%, respectively. However, it has less influence on  $\Delta\lambda_D$  and  $\Delta\lambda_0$ , relative deviation only 1%. The effects of calibration uncertainty on other parameters were also evaluated. The results show that the uncertainty does not affect the Doppler and turbulence velocities nor the line broadening, but does affect the column number density and temperature. The relative errors of  $N_i$ ,  $T_c$  and  $V_t$  are estimated to be about 13%, 8% and less than 1%, respectively (ref. Table 2).

$\text{H}\alpha$  profiles are usually very broad. For this flare, it is extraordinarily broad near the loop top (see Fig. 7b), with a width more than  $4 \text{\AA}$ . By the MCM method, the wide profile may be explained as a result of overlapping of two elementary profiles (labelled 1 and 2 in Fig. 7b) along the line-of-sight direction. In this case,  $\Delta\lambda_D$  is 2.392 and  $0.944 \text{\AA}$  for the two elementary profiles, respectively (see Table 1). In general, the broadening mechanism of the elementary profiles consists of two factors: thermal Doppler effect and non-thermal effect. When  $\Delta\lambda_D \geq 2 \text{\AA}$  (such as elementary profile 1), the thermal effect (the second term in Eq.(6)) is very small, which alone cannot explain the very wide elementary profile; hence, the non-thermal effects are important, which include micro-turbulence, inhomogeneous mass motions (Ding et al. 1999, Paper I) and electron beam bombardment (Fang et al. 2000).

It should be pointed out that the velocity computed with the method of profile weight center reflects an average Doppler velocity along the line of sight, while the velocity derived from the MCM method is the Doppler velocity in the ‘cloud’. For singly-peaked profiles, these two values are similar; however, they are different for profiles with multiple peaks. Obviously, in the latter case, the MCM method is more appropriate.

The solution of the MCM method is not mathematically unique, but we can reject the “unreasonable” solutions and retain the “reasonable” ones by checking the continuity of parameters along the loops (Gu et al. 1992). The continuity of parameters derived by the MCM method is confirmed from the distribution of parameters along the slit for the flare of 1981 May 16 (figs. 3 and 4 of Gu et al. 1997). The parameter continuity is also proved from the two-dimensional multi-parameter fields obtained from the limb flare of 1989 August 17 based on the MCM (see figs. 4 to 7 in Gu et al. 2001). For a given precision, the Doppler velocity and Doppler width are reliable, while the other quantities are approximate, the selected physical solution may be considered as being “approximately unique” in that sense.

We also note that the MCM does not properly take into account other factors which can affect the absolute intensity and the width of line profiles, such as incident radiation into the loop and the bombardment by non-thermal electrons. Thus, the results presented here may not be accurate where these factors are important. A more refined determination relies on full non-LTE computations. This will be done in a future work.

**Acknowledgements** One of the authors (X. M. Gu) would like to thank Dr. T. G. Forbes for giving financial support and helpful discussions during his visit to the University of New Hampshire, USA. M. D. Ding expresses his thanks to the Chinese Academy of Sciences and Yunnan Observatory for financial support of the Senior Visitor Program. We would also like to

express our appreciation to Dr. Q. Z. Qu and especially to Drs. K. J. Li and J. Lin for great helps in the computer code. In addition, the authors thank Dr. H. Hudson for providing the X-ray data of the flare observed by the *Yohkoh* satellite.

## References

- Beckers J. M., 1964, Ph. D. Thesis, Utrecht; AFCRL Env. Res. Papers, 49  
 Chen P. F., Fang C., Tang Y. H. et al., 1999, *ApJ*, 513, 516  
 Chen J., Lin Y. Z., 1987, *Acta Astrophys. Sin.*, 7, 287  
 Ding M. D., Fang C., Huang Y. R., 1995, *Solar Phys.*, 158, 81  
 Ding M. D., Fang C., Yin S. Y. et al., 1999, *A&A*, 348, L29 (Paper I)  
 Ding M. D., Fang C., 1997, *A&A*, 318, L17  
 Dun J. P., Gu X. M., Xuan J. Y., 1998, *Acta Astrophys. Sin.*, 18, 432  
 Dun J. P., Gu X. M., Zhong S. H., 2000, *Ap&SS*, 274, 473  
 Fang C., Henoux J.-C., Ding M. D., 2000, *A&A*, 360, 702  
 Fang C., Tang Y. H., Henoux J.-C. et al., 1998, *Solar Phys.*, 182, 163  
 Fang C., Feautrier N., Henoux J.-C., 1995, *A&A*, 297, 854  
 Gan W. Q., Rieger E., Fang C., 1993, *ApJ*, 416, 886  
 Gu X. M., Lin J., Li K. J., 1995, *Acta Astrophys. Sin.*, 15, 351  
 Gu X. M., Dun J. P., Zhong S. H., 2001, *A&A*, 380, 704  
 Gu X. M., Lin J., Luan T. et al., 1992, *A&A*, 259, 649  
 Gu X. M., Lin J., Li K. J. et al., 1994, *A&A*, 282, 240  
 Gu X. M., Ding Y. J., Luo Z. et al., 1997, *A&A*, 324, 289  
 Gu X. M., Lin J., Li K. J. et al., 1996, *Ap&SS*, 240, 263  
 Huang Y. R., Fang C., Ding M. D. et al., 1995, *Solar Phys.*, 159, 127  
 Heinzel P., Schmieder B., Mein P., 1992, *Solar Phys.*, 139, 81  
 Li K. J., Ding Y. J., 1992, *Acta Astron. Sin.*, 33, 171  
 Li K. J., Ding Y. J., Bai J. M. et al., 1994, *Solar Phys.*, 150, 87  
 Li K. J., Ding Y. J., Gu X. M. et al., 1993, *A&A*, 269, 496  
 Li K. J., Zhong S. H., Ding Y. J. et al., 1995, *A&AS*, 109, 347  
 Li K. J., Schmieder B., Malherbe J.-M. et al., 1998, *Solar Phys.*, 183, 323  
 Lin J., Forbes T. G., Priest E. R. et al., 1995, *Solar Phys.*, 159, 275  
 Mein P., Mein N., 1988, *A&A*, 203, 162  
 Mein P., Mein N., Malherbe J.-M. et al., 1997, *Solar Phys.*, 172, 161  
 Švestka Z. F., Fontenla J. M., Machado M. E. et al., 1987, *Solar Phys.*, 108, 237  
 Schmieder B., Shibata K., Van Driel-Gesztelyi L. et al., 1995a, *Solar Phys.*, 156, 245  
 Schmieder B., Heinzel P., Wiik J. E. et al., 1995b, *Solar Phys.*, 156, 337  
 Schmieder B., Heinzel P., van Driel-Gesztelyi L. et al., 1996, *Solar Phys.*, 165, 303  
 Van Driel-Gesztelyi L., Schmieder B., Cauzzi G. et al., 1996, *Solar Phys.*, 163, 145  
 Wiik J. E., Schmieder B., Heinzel P. et al., 1996, *Solar Phys.*, 166, 89  
 Ye S. H., Jin J. H., 1985, *Solar Phys.*, 96, 113  
 Zhong S. H., Cheng X. K., Luo Z., 1991, *Pub. of Yunnan Obs.*, No.2, 14  
 Zhong S. H., 1995, *Pub. of Yunnan Obs.*, No.3, 30